AGU ADVANCING EARTH AND SPACE SCIENCE

Water Resources Research

TECHNICAL REPORTS: METHODS

10.1029/2020WR029315

Enabling the Application of Large Footprint Open-Bottom Permeameters Through New Shape Factors

Vitaly A. Zlotnik[1], Kevin D. Cole[2], Meinhard B. Cardenas[3], and Anatoly V. Zlotnik[4]

[1]Department of Earth and Atmospheric Sciences, University of Nebraska-Lincoln, Lincoln, NE, USA, [2]Department of Mechanical and Materials Engineering, University of Nebraska-Lincoln, Lincoln, NE, USA, [3]Jackson School of Geosciences, University of Texas, Austin, TX, USA, [4]Applied Mathematics and Plasma Physics (T-5), Los Alamos National Laboratory, Los Alamos, NM, USA

Key Points:

- Open-bottom permeameters are used for studies of fluxes and sediment properties of surface water-groundwater interfaces
- Traits and advantages of large radii and shallow penetrations of permeameters are demonstrated using hydrodynamic analysis
- For applications, shape factor values are calculated and documented in the entire range of practically necessary parameters

Supporting Information:

Supporting Information may be found in the online version of this article.

Correspondence to:

V. A. Zlotnik,
vzlotnik1@unl.edu

Citation:

Zlotnik, V. A., Cole, K. D., Cardenas, M. B., & Zlotnik, A. V. (2021). Enabling the application of large footprint open-bottom permeameters through new shape factors. *Water Resources Research*, *57*, e2020WR029315. https://doi.org/10.1029/2020WR029315

Received 2 DEC 2020
Accepted 19 APR 2021

Abstract Open-bottom permeameters (OBP) are commonly used for estimating the hydraulic properties of sediment beds under water bodies and fluxes across the sediment-water interface. The specific shape factor for an OBP flow situation is necessary for data interpretation. It is determined by the ratio of the permeameter tube radius to the tube's penetration depth within the sediment. Previous permeameter designs favored small radii which allowed for deeper penetration and stability of the tube. The shape factor is provided here for large footprint OBPs that allows for shallow penetration and greater radius. Through a numerical and analytical modeling study of the OBP hydrodynamics, previous knowledge on the OBP shape factor is generalized to the entire range of radius-to-penetration ratios that might be practically applied. The results reveal the advantages of the large footprint design, including better sensitivity due to the ability to impose larger discharge over a shorter test duration.

Plain Language Summary Various instruments use open-bottom permeameters (OBP) for investigation of characteristics of the surface water-groundwater interfaces, for example by slug tests, seepage meter tests, and piezo-seep meter tests. Previously, typical designs favored small tube radii which allowed for deeper penetration and stability of the tubes. It is shown that large footprint instruments (with large tube radius-to-penetration ratios) may provide better sensitivity and practical advantages in various tests. A numerical and analytical modeling of the OBP hydrodynamics generalized the OBP shape factor necessary for data interpretation in the entire practical range of radius-to-penetration ratios.

1. Introduction

Open-bottom permeameters (OBP) are commonly used in investigations of surface water-groundwater interactions (e.g., Rosenberry et al., 2008; Zlotnik et al., 2016). Some applications include obtaining properties of the hyporheic zone, including hydraulic conductivity (Chen, 2000; Chen et al., 2009, 2011; Kelly & Murdoch, 2003; Vasilevskiy et al., 2019), fluxes across streambeds (e.g., Harvey & Wagner, 2000; Solder et al., 2016; Solomon et al., 2020) and lakebeds (e.g., Ong & Zlotnik, 2011), tidal effects (e.g., Liu et al., 2018), submarine groundwater discharge (Liu et al., 2018), and discharge into wetlands (Rosenberry & Hayashi, 2013). The OBP geometry is defined by the permeameter tube of radius R, inserted to depth L into the generally anisotropic sediment/aquifer with horizontal and vertical conductivity values K_r and K_z, respectively (Figure 1a). The lower part or the chamber of the tube is filled with the substrate material, while the upper part containing water is used for monitoring the water level under static or dynamic conditions. Typically, the total substrate thickness greatly exceeds the penetration depth. The upper water-holding chamber can sometimes amplify or accelerate flow within it by having a constricted radius R_S relative to the bottom sediment-penetrating chamber as shown in Figure 1b (Solder et al., 2016; Solomon et al., 2020).

If the head at the interface inside the tube (water level) exceeds the head (water level) at the stream-substrate interface by the value H, the water flux is directed from the upper chamber of the OBP through the lower chamber with the substrate sediments and out toward the interface. (The direction is opposite if the water level inside is lower than the water level outside). This OBP, like any other tube permeameter with different screen configurations (e.g., Bouwer, 1978; Cardenas & Zlotnik, 2005), creates a dipole-flow system between the upper chamber and the stream (e.g., Zlotnik & Ledder, 1996). Head distribution changes are

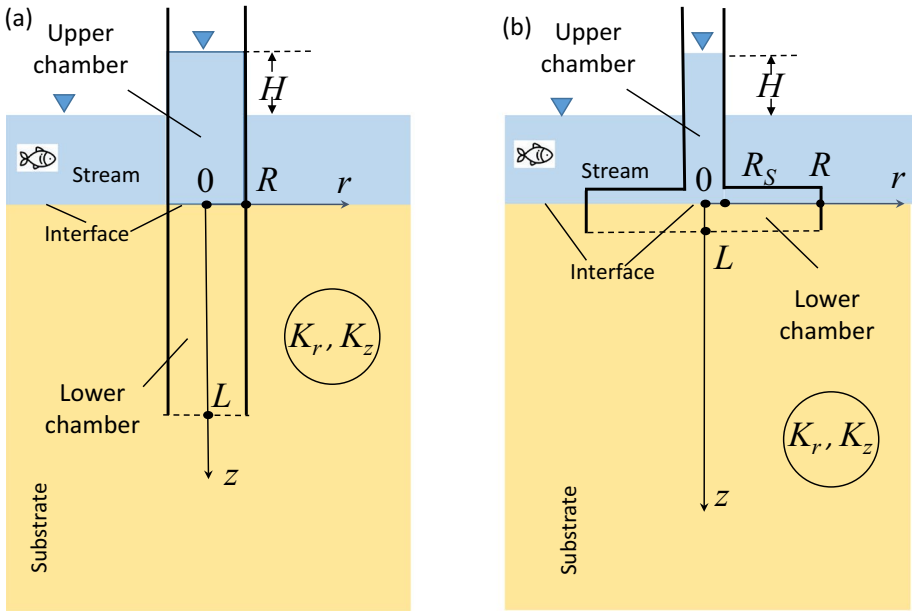

Figure 1. Schematic diagram of the OBP in the substrate: (a) small-radius footprint, (b) large-radius footprint with amplifier. OBP, open-bottom permeameters.

localized near this dipole; hence, the OBP is mainly sensitive to the hydraulic conductivity of the sediment inside the bottom chamber and within the chamber's immediate vicinity.

The steady-state discharge Q through the tube follows Darcy's equation modified for the flow geometry:

$$Q = \pi R^2 \frac{K_z H}{L F\left(R^*\right)}, \quad R^* = \frac{R}{L}\sqrt{\frac{K_z}{K_r}} \tag{1}$$

where $F\left(R^*\right)$ is the shape factor, which depends on a single dimensionless parameter R^*, defined by the substrate properties (K_r and K_z) and the OBP geometry (R and L). Physically, the shape factor indicates the magnitude of resistance of sediments to the flow outside of the lower chamber of the permeameter, in addition to the resistance of the bottom chamber. Value $F\left(R^*\right) = 1$ indicates that the resistance of sediments outside the bottom chamber can be neglected. (In the following text, we will use a shape factor F with subscripts to reconcile previously known notations).

The realistic range of parameter R^* can be assessed based on the OBP geometry in slug tests and flux measurements, considering the small scale anisotropy of the substrate. In general, the OBP tests are performed using elongated tubes with $R / L \leq 0.1$ (e.g., Chen et al., 2011; Landon et al., 2001). For flux measurements, this ratio may vary from approximately 0.15 (Solder et al., 2016; Solomon et al., 2020) for small footprint measurements to 15–30 for larger-footprint seepage meters made of metal barrels that are commonly used ($R = 0.3$ m) and penetration depth on the order of 0.01 m (Rosenberry et al., 2008). Values of small-scale anisotropy of hydraulic conductivity (K_r / K_z) in natural fluvial environments range from 1 to 10 (Burger & Belitz, 1997). Therefore, the practically important range of dimensionless radius is $0.01 < R^* < 100$.

For example, the shape factor ascribed to Hvorslev (1951) by Chen (2000), Landon et al. (2001), and others for tubes with small R / L ratio is as follows:

$$F_H\left(R^*\right) = 1 + \frac{\pi}{5.5} R^*, \tag{2}$$

where R^* is typically less than approximately 0.2. Considering practical applications with small R^*, one obtains $F_H \approx 1$, that is, the resistance of sediments outside the lower chamber to the flow is commonly

neglected (Chen et al., 2011). Paradoxically, the OBP design is absent from a compilation of different flow test geometries by Hvorslev (1951) where many similar configurations of the lower chamber and the perforated screens are presented. The needed OBP design was studied by Bouwer (1978, Table 5.6) using electrical analog models.

Considering the potential for broad application of the permeameter test, Pozdnyakov et al. (2016) revisited the OBP problem and proposed a more accurate shape factor as a function of R^* for the small footprint scenario:

$$F_P\left(R^*\right) = 1 + \frac{\pi}{5.6} R^* \left(1 - 0.243 \cdot f\right),$$
$$f\left(R^*\right) = \frac{2}{\pi} \sin^{-1}\left(\frac{R^* / 2}{\sqrt{0.0156 R^{*2} + 1} + \sqrt{0.7656 R^{*2} + 1}} \right) \tag{3}$$

Although the accuracy of this form was assessed by using a finite-difference flow model, the relative error as a function of R^* was not tabulated but we will show it below.

The significance of this parameter in surface water-groundwater interactions studies and in data interpretation is as follows: Various OBP-based tests register the responses of the water level $H\left(t\right)$ in the upper chamber. For example, in the falling head slug test, the water level recovery $H(t)$ in the upper chamber of the OBP (Figure 1a) after a rapid increase in water level there by the value H_0 (Freeze & Cherry, 1979; Hvorslev, 1951) is recorded. The water level reduces exponentially with time following $H\left(t\right) = H_0 \exp\left(-t / t_L\right)$. The term "time lag" for parameter t_L, determined by the chamber geometry and substrate properties was introduced by Hvorslev (1951):

$$t_L = LF / K_z \tag{4}$$

Calver (2001) considered the range for streambed hydraulic conductivity values between 0.01 m day^{-1} and 100 m day^{-1} as typical. For $L = 0.3$ m and $R = 0.05$ m that are typical of OBP applications in automated seepage meters (Solomon et al., 2020), $F \approx 1$ as discussed above. Thus, t_L may range from 5 min to 30 days. The commonly occurring large time lags can affect the feasibility of the test due to temporally fast changes in stream stage, tide level, etc. Reducing the time lag would be a major advantage which requires particular attention to selection of the instrument design (i.e., R and L).

One of the approaches to reduce this time lag is to add the amplifier mentioned above by using a smaller-radius tube R_S over the upper chamber (Figure 1b) for monitoring $H\left(t\right)$ (e.g., Solder et al., 2016). In this case, the adjusted time lag is

$$t_L = \frac{LF}{K_z} \left(\frac{R_S}{R} \right)^2 \tag{5}$$

The resulting increase in the footprint of the OBP typically reduces the penetration depth, resulting in changes to the ratio R / L and the value of R^*. In fact, such large footprint design could provide vertical stability of the OBP in different environments. While such design makes OBP tests more feasible, the shape factor values for the range $0.1 < R^* < 100$ have not been reported. Determining the shape factor $F\left(R^*\right)$ as a function of R^* is the primary goal of this note.

Using finite element flow modeling and analytical techniques, we provide a simple solution for both theoretical and practical purposes, including the design of various instruments. The focus here is on hydrological applications with attention on changes in discharge and time lag; the complete technical details are presented as supporting information.

2. Statement of the Boundary Value Problem

Due to the small vertical and horizontal scales of the dipole system, one can neglect the compressibility effects in the volume inside and outside the OBP in the groundwater flow equation:

$$\frac{K_r}{r}\frac{\partial}{\partial r}\left(r\frac{\partial h}{\partial r}\right)+K_z\frac{\partial^2 h}{\partial z^2}=0,\quad r>0,\ z>0 \tag{6}$$

The boundary condition at the interface indicates the difference between the head inside and outside the OBP:

$$h(r,0)=\begin{cases}0, & R<r<\infty\\ H, & 0<r<R\end{cases} \tag{7}$$

The walls of the tube are impermeable:

$$\frac{\partial h(R,z)}{\partial r}=0,\quad 0<z<L \tag{8}$$

The boundary condition at z-axis indicates axial symmetry as follows:

$$\frac{\partial h(0,z)}{\partial r}=0,\quad 0<z<\infty \tag{9}$$

and the function with derivatives vanishes far from the OBP:

$$\lim_{r^2+z^2\to\infty} h(r,z)=0 \tag{10}$$

Discharge is evaluated by summing up the fluxes across the interface $z=0$ inside the upper chamber:

$$Q=K_z\frac{H}{LF}\left(\pi R^2\right)=2\pi K_z\int_0^R\frac{\partial h(r,0)}{\partial z}rdr \tag{11}$$

Thereby, the problem of finding the dimensionless shape factor F in Equation 1 is reduced to determination of the flux Q:

$$F=\frac{\pi K_z H R^2\ /\ L}{Q} \tag{12}$$

3. Dimensionless Variables

Dimensionless coordinates ($r^*,\ z^*$), OBP radius (R^*), and head (h^*)

$$r^*=\frac{r}{L}\sqrt{\frac{K_z}{K_r}},\quad z^*=\frac{z}{L},\quad R^*=\frac{R}{L}\sqrt{\frac{K_z}{K_r}},\quad h^*=\frac{h(r^*,z^*)}{H} \tag{13}$$

are applied to transform the boundary value problem as follows:

$$\frac{1}{r^*}\frac{\partial}{\partial r^*}\left(r^*\frac{\partial h^*}{\partial r^*}\right)+\frac{\partial^2 h^*}{\partial z^{*2}}=0,\quad r^*>0,\ z^*>0 \tag{14}$$

$$h^*(r^*,0)=\begin{cases}1, & 0\le r^*<R^*\\ 0, & r^*<R^*<\infty\end{cases} \tag{15}$$

Table 1
The OBP Shape Factors $F\left(R^*\right)$ and $F_I\left(R^*\right)$

R^*	$Q^*(R^*)$	$F(R^*)$	$F_I(R^*)$
0.01	0.00031229	1.006	1.008
0.05	0.0076291	1.029	1.040
0.075	0.016919	1.044	1.058
0.1	0.029651	1.059	1.077
0.2	0.1125	1.117	1.146
0.3	0.24107	1.173	1.211
0.4	0.40953	1.227	1.273
0.5	0.61325	1.281	1.333
0.6	0.84839	1.333	1.392
0.7	1.1117	1.385	1.449
0.8	1.4007	1.435	1.505
0.9	1.7129	1.486	1.559
1	2.0464	1.535	1.613
2	6.2816	2.000	2.114
3	11.627	2.432	2.571
5	24.323	3.229	3.412
8	46.551	4.319	4.565
10	62.846	4.999	5.287
15	108.41	6.520	6.990
20	155.87	8.062	8.593
40	367.31	13.684	14.455
50	481.68	16.304	17.188
70	721.58	21.332	22.414
80	845.76	23.771	24.938
100	1,102	28.506	29.851

$$\frac{\partial h^*\left(R^*,z^*\right)}{\partial r^*}=0,\quad 0<z^*<1 \tag{16}$$

$$\frac{\partial h^*\left(0,z^*\right)}{\partial r^*}=0,\quad 0<z^*<\infty \tag{17}$$

$$\lim_{r^{*2}+z^{*2}\to\infty} h^*\left(r^*,z^*\right)=0 \tag{18}$$

The discharge in dimensionless coordinates Q^* depends on one parameter R^*:

$$Q^*\left(R^*\right)=2\pi\int_0^{R^*}\frac{\partial h^*\left(r^*,0\right)}{\partial z^*}r^*dr^* \tag{19}$$

The dimensional injection rate Q is related to Q^* as follows:

$$Q=K_rHLQ^*\left(R^*\right) \tag{20}$$

Equation 12 for the shape factor now depends on the dimensionless radius R^* only:

$$F\left(R^*\right)=\frac{\pi K_zHR^2\ /\ L}{Q}=\frac{\pi K_zHR^2\ /\ L}{K_rHLQ^*}=\frac{\pi}{Q^*}\left(\frac{R}{L}\sqrt{\frac{K_z}{K_r}}\right)^2=\frac{\pi R^{*2}}{Q^*\left(R^*\right)} \tag{21}$$

4. Computation of the Shape Factor Using Numerical Modeling

The definition following Equation 21 permits a straightforward evaluation of the shape factor by numerical methods when the boundary value problem 10–14 in dimensionless variables is solved for various values of the parameter R^*. We used the finite element approach implemented in COMSOL Multiphysics, a commercial software. This method requires constraining the semi-infinite domain in Equation 14 radially and vertically to the finite domain.

The following approach was used considering that OBP fluxes are similar to the dipole where the source of water in the upper chamber is balanced by the sink distributed across the stream-streambed interface outside the OBP and vice versa. Head and velocity magnitude variations outside the lower OBP chamber decay very rapidly in all directions. Therefore, we limited our domain vertically by $0\le z^*\le 10$ and by $0\le R^*\le 10R^*$ horizontally. Details on selecting the mesh size are available in Text S1.

The dimensionless function $Q^*\left(R^*\right)$ was calculated by discretized Equation 19 within the COMSOL Multiphysics and presented in Table 1. The accuracy of the numerical solution was almost unaffected by the increasing size of the computational finite domain and the reduction of mesh size. In particular, the difference between dipole fluxes across the interface (inside the OBP permeameter and outside) was on the order of 0.1% at any R^* (Text S1).

The corresponding shape factor $F(R^*)$ was calculated from $Q^*\left(R^*\right)$ using Equation 21 and given in Table 1 and Figure 2. For comparison, shape factors by Hvorslev (1951), denoted F_H and Pozdnyakov et al. (2016), and denoted F_P are depicted, showing their narrow range of validity based on the desired accuracy of 5%.

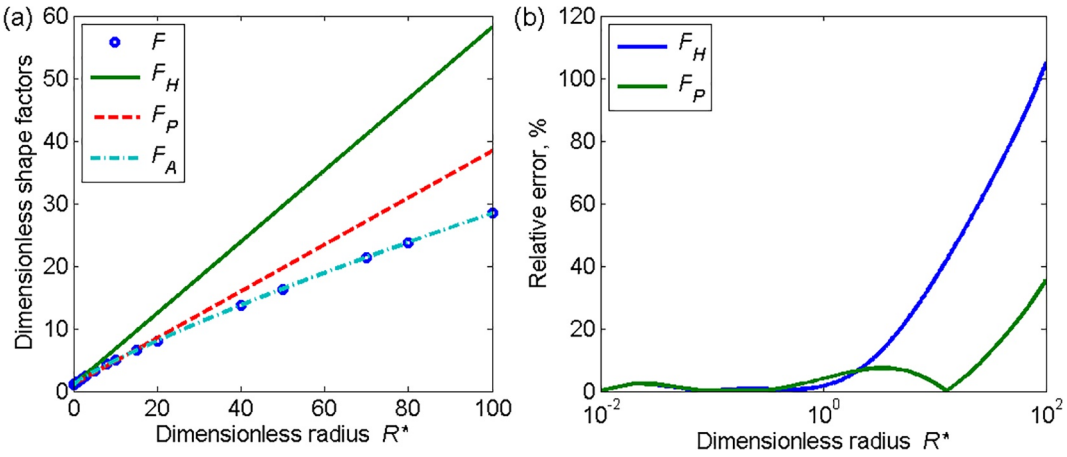

Figure 2. Shape factor (F): (a) comparison of numerically estimated shape factor F with previously published results; F_H – Hvorslev (1951) shape factor, F_P – Pozdnyakov et al. (2016), F_A – shape factor approximation based on numerical modeling results; and (b) relative accuracy of previously used shape factors.

To assist with practical applications, the function $F\left(R^*\right)$ in Table 1 was approximated by the function $F_A\left(R^*\right)$, using elementary functions with accuracy better than 1%:

$$F_A\left(R^*\right) = \exp[0.435710 + 0.326818 * \ln\left(R^*\right) + 0.0786683 * \left(\ln\left(R^*\right)\right)^2 + 0.00169158 * \left(\ln\left(R^*\right)\right)^3 - 0.00095506 * \left(\ln\left(R^*\right)\right)^4] \quad (22)$$

as explained in Text S2 (A better approximation can be achieved if needed by shortening the range of R^*). The approximation $F_A\left(R^*\right)$ virtually coincides with the numerical model determined result $F(R^*)$ in Figure 2a. Note that the relative errors in shape factors $F_H\left(R^*\right)$ and $F_P\left(R^*\right)$ increase rapidly with $R/L > 3$, but $F_P\left(R^*\right)$ is applicable in a greater range if the accuracy requirements are about 5%–8% (Figure 2b).

5. Analytical Estimate of the Shape Factor

The numerical model results gave a clear presentation of data for fixed values of parameters in the expected ranges. However, analytical solutions can provide trends that are beyond these ranges. An accurate solution of the problem with Equations 6–10 is possible by splitting the flow domain into subdomains, then determining the solution in each one while imposing the continuity of head and flux on each interface (Cole et al., 2011, Ch. 12). However, the resulting solution involves numerous poorly convergent integrals and does not offer practical advantages over numerical modeling results such as above. Previously, all approximations of shape factors were developed for low values of R^*. We explored solutions for similar geometry with high values of R^*. The limiting case of such an analytical solution was presented by Bruggeman (1999, p.369) in a compact form or in a more general form, but it was presented in a more complicated form by Tartakovsky et al. (2000). They utilized a first type boundary condition equivalent to Equation 7. However, it was found that application of these solutions for deriving shape factors based on definitions in Equations 11 and 12 above results in a singular solution involving divergent integrals.

Our modification of the problem centers on the role of the OBP's lower chamber and is based on the analyses of R^* values. This chamber has a very short length L compared to R, which results in small resistance to the flux of the lower chamber. Then, the boundary condition Equation 7 can be written as follows:

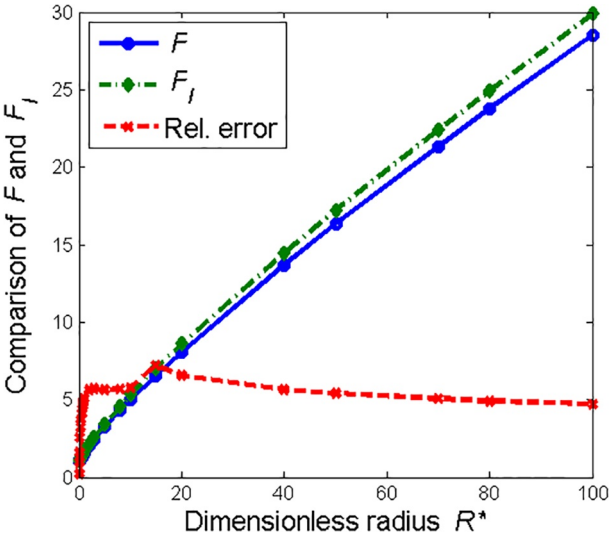

Figure 3. Comparison of approximate analytical (F_I) and accurate (F) shape factors (left vertical axis). The relative error $|F_I - F| / F$ is shown on the right vertical axis.

$$-K_z \frac{\partial h(r,0)}{\partial z} = \frac{K_z}{L}\begin{cases} h(r,0) - H, & 0 < r < R \\ h(r,0), & R < r < \infty \end{cases} \tag{23}$$

where the right-hand side divided by the small finite parameter L is large compared to the left-hand side and the left-hand side is negligibly small. Thus, this boundary condition is close to the original Equation 7, while the left-hand side serves for improvement of convergence of solutions after substituting into Equations 11 and 12. These approximations obviate the need for the zero-flux boundary condition in Equation 8 but allow for retaining the effect of hydraulic resistance of sediments in the lower chamber to the flow. More details can be found in Text S3.

The purpose of this solution is the availability of reasonable head estimates (to be shown below) and Stokes stream functions. This regularization approach of the problem could be assessed using perturbation methods (Bender & Orszag, 1999). Instead, we will compare it with numerical model results summarized by $F_A(R^*)$ in Equation 22.

The corresponding solution of the problem 6, 9, 10 and 23 by Green's function technique was constructed from the Hankel transform procedure (Cole et al., 2011) and explained in Text S3. In our notation, it is as follows:

$$h(r,z) = HR^* \int_0^\infty \frac{e^{-\beta z^*}}{\beta + 1} J_0(\beta R^*) J_1(\beta R^*) d\beta \tag{24}$$

From here, flux through the lower OBP chamber, defined by Equation 11, can be calculated using Equation 23, dimensionless variables by Equation 13, and definition of dimensionless flux in Equation 19 (Cole, 2020):

$$Q = 2\pi \int_0^R \frac{K_z}{L}\left[H - h(r,0)\right] r dr = K_r L H \cdot Q^*, \tag{25}$$

where the dimensionless flux Q^* is equal to Q_I^*, containing infinite domain integral as follows:

$$Q_I^*(R^*) = \pi R^{*2}\left[1 - 2\int_0^\infty \frac{\left[J_1(\beta R^*)\right]^2}{\beta(\beta+1)} d\beta\right] \tag{26}$$

(Here, identity $\int x J_0(x) dx = x J_1(x)$ is used after Abramowitz and Stegun, 1965, Equation 11.3.20). The shape factor, denoted as F_I, is calculated according to the definition in Equation 21:

$$F_I(R^*) = \left[1 - 2\int_0^\infty \frac{\left[J_1(\beta R^*)\right]^2}{\beta(\beta+1)} d\beta\right]^{-1} \tag{27}$$

The integration converges slowly because of the oscillating nature of the integrand (e.g., Ledder & Zlotnik, 2017) and the results are shown in Table 1 for comparison. This shape factor F_I in Figure 3 is compared with the shape factor F_A (see the left axis), and the relative error is shown on the right axis. The Matlab script for calculations is given in Text S4. Function F_I provides adequate approximation of numerical results in the entire practical range of R^*, if 5% error is acceptable. Moreover, the asymptotic behavior seems to be behaving as $O(R^* \cdot \ln R^*)$ at large values.

This solution can be used for determining the point head values and flownet construction in various applications of OBP.

6. Discussion and Summary

The results of our analyses show the limitations of the traditional view on OBP test interpretation and provide their remediation. Indeed, Equation 1 shows that the one-dimensional Darcy's law is applicable to the interpretation of data only for designs with a small footprint R/L because the shape factor F may exceed 1 significantly. For a small footprint, the hydraulic resistance of sediments in the substrate around the lower chamber can be neglected compared to the one inside the lower chamber; for a large footprint, the fraction of substrate resistance around the lower chamber vastly exceeds the resistance of sample in the lower chamber.

The physical reason for this behavior in F is the structure of the flow inside the lower chamber. For $R << L$, the flow in the chamber is near-uniform and one-dimensional. For $R >> L$, the short chamber creates a nonuniform and three-dimensional flow with a large horizontal velocity component (see also Kelly & Murdoch, 2003). Therefore, Equations 4 and 5 offer three possible modifications of OBP configuration: Smaller penetration, larger radius, and using the amplifier (Figure 1b above and Solder et al., 2016).

The shape factor F depends on the radius-to-penetration ratio R / L. Thus, according to Equation 1, an increase in R may not necessarily produce a quadratic increase in discharge Q, and a decrease in L may not necessarily produce an inversely proportional Q increase as it could follow for Darcy's interpretation of OBP tests. (It is assumed that H, K_r, and K_z are fixed at the test location, when different instruments are used.) To compare the discharge from two configurations (parameters L_1, R_1, and discharge Q_1, and parameters L_2, R_2, and discharge Q_2) the following expression follows from Equations 20 and 21 at a given interface location:

$$\frac{Q_2}{Q_1} = \frac{L_2}{L_1}\frac{Q*\left(R_2^*\right)}{Q*\left(R_1^*\right)} = \left(\frac{R_2^*}{R_1^*}\right)^2 \frac{L_2}{L_1}\frac{F\left(R_1^*\right)}{F\left(R_2^*\right)} \tag{28}$$

where $Q^*\left(R^*\right)$ and $F\left(R^*\right)$ are calculated in Equation 22. This discharge ratio Q_2 / Q_1 significantly differs from an estimate, which ignores the flow's three-dimensionality when $F\left(R_1^*\right) = F\left(R_2^*\right) = 1$.

We illustrate the point by comparison of fluxes (seepage rate) measured by two different instruments in an anisotropic aquifer. One instrument has a small footprint and dimensions of a seepage meter described by Solder et al. (2016) or Solomon et al. (2020): $L_1 = 0.3$ m and $R = 7.5$ cm, with $R/L = 0.25$. The alternative is the footprint of typical seepage meters (Rosenberry et al., 2008), made of a standard oil barrel with radius $R_2 = 30$ cm and shallow penetration $L_2 = 3$ cm, resulting in $R^* = R/L = 10$. If the flow in the lower chamber is considered as one-dimensional in Equation 26 and the identity $F\left(R_1^*\right) = F\left(R_2^*\right) = 1$ is assumed, the gain in discharge is Q_2 / Q_1 = 160. However, consideration of three-dimensionality produces the corrected gain Q_2 / Q_1 = 60 that should be considered in the design of the OBP.

Another important use of the obtained theoretical results is an ability to control and design the time lag of the instruments. OBP tests (slug tests and flux measurements using seepage meters) can sometimes require significant time to conclude. In these cases, the design of the instrument can be modified to reduce time lag, that is, $\left(t_L\right)_2 < \left(t_L\right)_1$.

$$\frac{\left(t_L\right)_2}{\left(t_L\right)_1} = \frac{L_2}{L_1}\frac{F\left(R_2^*\right)}{F\left(R_1^*\right)}\left(\frac{R_S}{R}\right)^2 \tag{29}$$

The same instruments can be used for illustration. Without an amplifier (i.e., $R_S = R$), the time lag is decreased by a factor of 3.8. If an amplifier with $R_S = 7.5$ cm is used (which is consistent with existing designs), the time lag reduction gains a factor of $(30.0/7.5)^2 = 16$. The test acceleration can be characterized by the value $\left(t_L\right)_2$ / $\left(t_L\right)_1$, which is approximately 61.

Finally, the results of this study can be applied to the design of new tests and refinement or modification of existing procedures. For example, the piezo-seep test for measurements of K_z proposed by Kelly and Murdoch (2003, Figure 4) combined the pumping discharge Q from the sealed-at-the-top upper chamber and by taking the head difference between the upper chamber and a single streambed point at the axis ($r = 0$). The point location must obey the additional constraint ($z < 0.8\ L$) to have 1D flow in the lower chamber. However, this coefficient 0.8 is not universal. It depends on R/L, which may play an important role in data interpretation. Reliance on a single head reading may introduce significant bias in K_z values compared to other methods. To avoid reliance on a single point head, a piezomanometer could be repurposed for finding the head difference between the upper chamber and the stream (see also Solder et al., 2016). Then, K_z could be found from Equation 1 as $K_z = QLF / \left(\pi R^2 H\right)$, where the shape factor accounts for the head distribution in its entirety and explicitly considers OBP geometry.

It should be noted that all these estimates implicitly assume perfect knowledge of test geometry, precise procedures, and homogeneity of streambed parameters. In fact, these characteristics have different violations of these assumptions, and sensitivity analyses to various parameters based on error propagation is recommended (see example in Text S5). Unfortunately, it is rare to see studies on the role of "noise" in the test data interpretations based on OBP.

These conclusions illustrate various practical ramifications for ubiquitous applications of OBP. In the past, streambed tests were performed with a small footprint due to the need to provide the vertical stability of the test tube, whether for hydraulic conductivity or for flux measurements. In many cases, this resulted in using small discharge values in OBP-based tests, causing test times to be excessive and limiting test feasibility in highly transient environments (e.g., streams, estuaries, and tide-influenced zones).

In summary, the theoretical analysis of the OBP shape factor suggests and enables possible test modifications by increases in footprint and reductions in penetration. These modifications also reduce time lag, thereby increasing the feasibility of these tests in dynamic settings.

Data Availability Statement

Data were not used, nor created for this research study.

Acknowledgments
The research study was partially supported by the NSF grant EAR 1744719. The authors acknowledge the contribution of Glenn Ledder (UNL) for participating in analyses of asymptotic behavior of the analytical solution.

References

Abramowitz, M., & Stegun, I. (1965). Handbook of mathematical functions: With formulas, graphs, and mathematical tables. In National Bureau of Standards, Applied Mathematics Series (Vol. 55). U. S. Government Printing Office.

Bender, C. M., & Orszag, S. A. (1999). *Advanced mathematical methods for scientists and engineers*. Springer-Verlag. https://doi.org/10.1007/978-1-4757-3069-2

Bouwer, H. (1978). *Groundwater hydrology*. McGraw-Hill.

Bruggeman, G. A. (1999). *Analytical solutions of geohydrological problems* (Vol. 46). Elsevier.

Burger, R. L., & Belitz, K. (1997). Measurement of anisotropic hydraulic conductivity in unconsolidated sands: A case study from a shoreface deposit, Oyster, Virginia. *Water Resources Research*, *33*(6), 1515–1522. https://doi.org/10.1029/97wr00570

Calver, A. (2001). Riverbed permeabilities: Information from pooled data. *Groundwater*, *39*(4), 546–553. https://doi.org/10.1111/j.1745-6584.2001.tb02343.x

Cardenas, M. B., & Zlotnik, V. A. (2005). A simple constant-head injection test for streambed hydraulic conductivity estimation. *Groundwater*, *41*(6), 867–871.

Chen, X. (2000). Measurement of streambed hydraulic conductivity and its anisotropy. *Environmental Geology*, *39*(12), 1317–1324. https://doi.org/10.1007/s002540000172

Chen, X., Song, J., Cheng, C., & Wang, D. (2011). Hydraulic conductivity along the Platte River, Nebraska. *Water Resources Management*, *25*, 265–285.

Chen, X., Song, J., Cheng, C., Wang, D., Lackey, S. O., & Song, J. (2009). A new method for mapping variability in vertical seepage flux in streambeds. *Hydrogeology Journal*, *17*(10), 519–525. https://doi.org/10.1007/s10040-008-0384-0

Cole, K., Beck, J., Haji-Sheikh, A., & Litkouhi, B. (2011). *Heat conduction using Greens functions*. Taylor and Francis.

Cole, K. D. (2020). R00Z30B5, steady axisymmetric heat transfer in a semi-infinite body with a surface conductance and piecewise fluid temperature. *Exact Analytical Conduction Toolbox*. Retrieved from https://exact.unl.edu

Freeze, R. A., & Cherry, J. A. (1979). *Groundwater* (p. 604). Prentice-Hall.

Harvey, J. W., & Wagner, B. J. (2000). *Quantifying hydrologic interactions between steams and their subsurface hyporheic zones in streams and ground waters* (pp. 3–44). Academic. https://doi.org/10.1016/b978-012389845-6/50002-8

Hvorslev, M. J. (1951). Time lag and soil permeability in groundwater observations. *Waterways Experiment Station, Corps of Engineers, U.S. Army*, Bulletin No. 36.

Kelly, S. E., & Murdoch, L. C. (2003). Measuring the hydraulic conductivity of shallow submerged sediments. *Groundwater*, *41*(4), 431–439.

Landon, M. K., Rus, D. L., & Harvey, F. E. (2001). Comparison of instream methods for measuring hydraulic conductivity in sandy streambeds. *Groundwater*, *39*(6), 870–885. https://doi.org/10.1111/j.1745-6584.2001.tb02475.x

Ledder, G., & Zlotnik, V. A. (2017). Evaluation of oscillatory integrals for analytical groundwater flow and mass transport models. *Advances in Water Resources*, *104*, 284–292. https://doi.org/10.1016/j.advwatres.2017.04.007

Liu, Y., Jiao, J. J., & Cheng, H. K. (2018). Tracing submarine groundwater discharge flux in Tolo Harbor, Hong Kong (China). *Hydrogeology Journal*, *26*, 1857–1873. https://doi.org/10.1007/s10040-018-1736-z

Ong, J. B., and V. A. Zlotnik, (2011). Assessing lakebed hydraulic conductivity and seepage flux by potentiomanometer. *Groundwater*. 2011, *49*(2), 270–274. https://doi.org/10.1111/j.1745-6584.2010.00717.x

Pozdnyakov, S. P., Wang, P., & Lekhov, M. (2016). A semi-analytical generalized Hvorslev formula for estimating riverbed hydraulic conductivity with an open-ended standpipe permeameter. *Journal of Hydrology*, *540*, 736–743.

Rosenberry, D. O., & Hayashi, M. (2013). Assessing and measuring wetland hydrology. In J. S. Anderson, & D. A. Davis (Eds.), *Wetland Techniques, 1: Foundations*. Springer.

Rosenberry, D. O., LaBaugh, J. W., & Hunt, R. J. (2008). Use of monitoring wells, portable piezometers, and seepage meters to quantify flow between surface water and ground water, Ch.2, in field techniques for estimating water fluxes between surface water and ground water. In D. O. Rosenberry, & J. W. LaBaugh (Eds.), *Techniques and Methods Chapter 4–D2*. U.S. Department of the Interior, U.S. Geological Survey. https://doi.org/10.3133/tm4d2

Solder, J. E., Gilmore, T. E., Genereux, D. P., & Solomon, D. K. (2016). A tube seepage meter for in situ measurement of seepage rate and groundwater sampling. *Groundwater*, *54*(4), 588–595. https://doi.org/10.1111/gwat.12388

Solomon, D. K., Humphrey, E., Gilmore, T. E., Genereux, D. P., & Zlotnik, V. (2020). An automated seepage meter for streams and lakes. *Water Resources Research*, *56*(4). https://doi.org/10.1029/2019WR026983

Tartakovsky, D. M., Moulton, J. D., & Zlotnik, V. A. (2000). Kinematic structure of minipermeameter flow. *Water Resources Research*, *36*(9), 2433–2442. https://doi.org/10.1029/2000wr900178

Vasilevskiy, P. Y., Wang, P., Pozdniakov, S. P., & Davis, P. (2019). Revisiting the modified Hvorslev formula to account for the dynamic process of streambed clogging: Field validation. *Journal of Hydrology*, *568*, 862–866. https://doi.org/10.1016/j.jhydrol.2018.11.034

Zlotnik, V. A., & Ledder, G. (1996). Theory of dipole flow in uniform anisotropic aquifers. *Water Resources Research*, *32*(3), 1119–1128. https://doi.org/10.1029/95wr03813

Zlotnik, V. A., Ward, A., Harvey, J., Lautz, L., Rosenberry, D., & Brunner, P. (2016). Ch. 9. Groundwater-surface water interactions. In J. Cushman, & D. Tartakovsky (Eds.), *Handbook of Groundwater Engineering* (3rd ed., pp. 237–288). Taylor and Francis.